Performance Analysis of Induction-Based Reaction Spheres

Zhu, Linyu; Guo, Jian; Gill, Eberhard

DOI
10.1109/TIE.2019.2946544

Publication date
2019

Document Version
Final published version

Published in
IEEE Transactions on Industrial Electronics

Citation (APA)
Zhu, L., Guo, J., & Gill, E. (2019). Performance Analysis of Induction-Based Reaction Spheres. *IEEE Transactions on Industrial Electronics*, *67 (2020)*(9), 7746-7756. Article 8870246.
https://doi.org/10.1109/TIE.2019.2946544

Performance Analysis of Induction-Based Reaction Spheres

Linyu Zhu, Jian Guo, and Eberhard Gill

***Abstract*—Induction-based reaction spheres have been presented in many references and their performances are normally investigated through experiments or numerical simulations which are time-consuming. Here, an analytical way is presented and it enables researchers to evaluate a new design quickly. In this article, the presented performance analysis is conducted through the classical equivalent circuit approach. Involved circuit parameters are determined through the magnetic flux density distribution which is a function of design variables. Based on this, the steady-state torque–speed curve and the achievable maximum driving torque T^* are identified. T^* deviates from the maximum torque obtained from numerical simulations by only 3%. For validation, the presented performance analysis method is applied to an experimental case. Mean absolute percentage errors of predicted torque–speed curves are within 23% and mainly caused by end effects. The presented performance analysis method is generally applicable to induction-based spherical actuators, not only limited to reaction spheres. Additionally, since influences of design variables of the actuator have been formulated analytically through the determined circuit parameters, performance optimizations could be greatly facilitated.**

***Index Terms*—Electromagnetic induction, parameter determination, reaction sphere.**

I. INTRODUCTION

IN RECENT years, small spacecraft have become more and more popular because of their low cost and short development times. Meanwhile, limited volume and power budgets of small spacecraft trigger the miniaturization of onboard components. In this context, reaction spheres are proposed as a replacement of reaction wheels. For typical spacecraft attitude control, at least three wheels are required to achieve three-axis stabilizations. However, reaction spheres can rotate and output control torques about any desired axis [1]–[3]. Therefore, if not considering redundancy, a single reaction sphere is sufficient for three-axis attitude control of spacecraft.

To enable multidimensional rotations, the driving unit of a reaction sphere is generally based on permanent magnets (PMs), electromagnetic induction or piezo/ultrasonic motors [1], [4]. Compared to the first two types, the piezo/ultrasonic-based reaction spheres have a low maximum speed (within 100 r/min), which means a highly limited momentum storage capability. In PM-based reaction spheres, torques are generated by interactions between PMs placed on the rotor and energized stator coils. Since the torque generation depends on the transient rotor orientation, which is obtained through measurements or estimations, control of the reaction sphere requires complicated coil switching strategies. Besides, measurements, data processing and complicated control strategies cause time delays in the real-time operations. On the contrary, induction-based reaction spheres have no fixed poles on the rotor, which means the orientation measurements/estimations are avoided. Therefore, a large number of reaction sphere designs belong to this type [1].

In induction-based reaction spheres, multiple sets of ac windings are placed around the conductive rotor and are controlled independently. As per vector superposition, the generated driving torque can be about any desired direction [5]–[7]. This concept was first proposed in [8] for the stabilizability of space telescopes. Its feasibility was studied through experiments of single-axis rotations in [9] and multiaxis rotations in [10]. Regarding performance analysis, current research works normally focus on the case of single-axis rotations to minimize the effects of cross couplings. In [11], torque–speed characteristics of a single-axis spinning reaction sphere were investigated through experiments on a prototype. To save development cost and allow researchers to evaluate designs before prototyping, Zhang *et al.* [12], Yan *et al.* [13] employed numerical simulations to examine performance characteristics as well as their dependencies on design variables. However, dynamic simulations of a three-dimensional (3-D) finite-element model (FEM) are time-consuming and require a large amount of memory [14]. Besides, the required time and memory amount increases rapidly when finer meshes or smaller time-step sizes are adopted [15]. To solve this problem, this article presents an analytical way to model the influences of design variables on the actuator performance characteristics.

Due to the resemblance between the single-axis rotation of induction-based reaction spheres and that of conventional induction machines, the equivalent circuit approach is employed to predict driving performances. Circuit parameters are determined through the magnetic flux density distribution, which is an analytical function of the design variables. Based on this,

---

Manuscript received November 26, 2018; revised March 17, 2019, June 11, 2019, and September 4, 2019; accepted September 25, 2019. Date of publication October 15, 2019; date of current version April 30, 2020. The work of L. Zhu was supported by China Scholarship Council. *(Corresponding author: Jian Guo.)*

The authors are with the Faculty of Aerospace Engineering, Delft University of Technology, 2629HS Delft, The Netherlands (e-mail: l.zhu@tudelft.nl; j.guo@tudelft.nl; e.k.a.gill@tudelft.nl).

Color versions of one or more of the figures in this article are available online at http://ieeexplore.ieee.org.

Digital Object Identifier 10.1109/TIE.2019.2946544

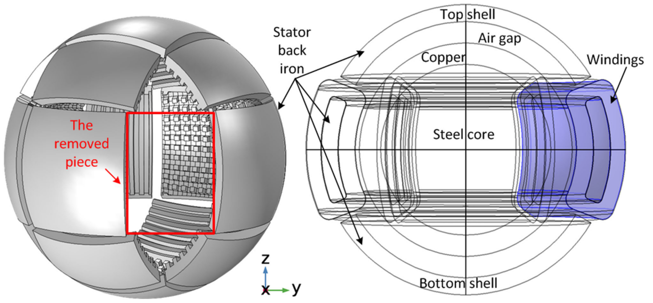

Fig. 1. Structures of the induction-based reaction sphere.

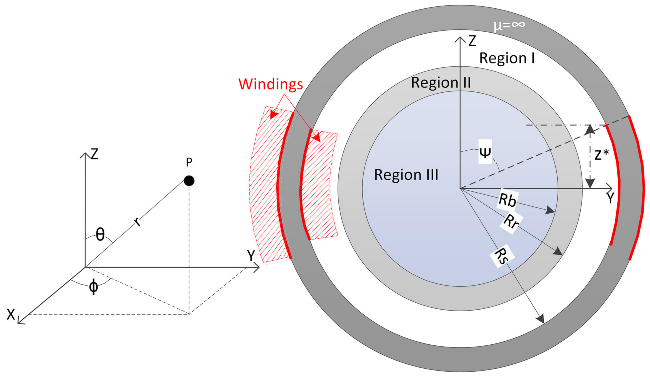

Fig. 2. Simplified geometry of the reaction sphere (Region I: air gap; Region II: copper; Region III: ferromagnetic core).

performance characteristics such as the achievable maximum torque T^* can be calculated within seconds. For validation, the proposed performance analysis method is applied to an experimental case. Mean absolute percentage errors of predicted torque–speed curves are within 23% and mainly contributed by end effects.

The performance analysis method presented in this article helps researchers to evaluate a new design quickly, with a low cost. Different from numerical simulations and prototype experiments, it allows input parameters of the design to be changed easily and gives corresponding results in seconds or minutes. Therefore, a design modification or optimization process can be greatly facilitated. Additionally, the presented performance analysis method is generally applicable to induction-based spherical actuators, such as robotic joints.

Normally, an induction-based reaction sphere incorporates ball bearings or magnetic bearings if additional stator coils/windings are mounted. The challenge of employing magnetic bearings is the cross-coupling between the suspension and the driving functions, and consequent disturbance forces/torques. In such cases, control of the reaction sphere becomes complicated. The cross-coupling and disturbances brought by magnetic bearings can be avoided by employing air bearings or ball bearings. Air bearings are popular in ground experiments and they facilitate functional tests of the driving unit. However, employing air bearings in space is difficult. Therefore, ball bearing is the preferred choice in this project. Although ball bearings introduce frictions and require lubrication, these drawbacks can be overcome by properly selected ball material and lubricants.

In the following, the dynamic magnetic field excited by three-phase stator windings is modeled analytically in Section II. Based on the obtained flux density distribution, equivalent circuit parameters are determined in Section III. The steady-state torque–speed curve and T^* are then identified. In Section IV, the proposed performance analysis method is applied to an actuator, which is designed for robotic applications. Predicted torque–speed curves are compared to the experimental data. Section V concludes this article.

II. FLUX DENSITY DISTRIBUTION

Fig. 1 illustrates structures of the studied reaction sphere. Please note that the presented design is just a basic design of induction-based reaction spheres. It is studied here to derive the field and equivalent circuit models, which can be generally applied to induction-based spherical actuators. To reduce the axial length, stator windings are toroidally wound on the back iron. Three sets of windings are placed on three principle axes to excite multidimensional rotations. On the left-hand side of Fig. 1, assembled stator segments are shown with one piece removed. Slots on the stator inner surface do not actually exist but they are drawn here to illustrate directions of wound wires. At joints of two winding sets, wires along different directions are wound on the same stator segment. Since this article focuses on the single-axis rotation, the structure shown on the right-hand side of Fig. 1 is adopted. Windings placed about the z-axis (in the stator frame) are energized to excite rotations while unenergized windings are replaced by the top/bottom shell. On the rotor, the steel core is covered with a copper layer. To facilitate analytical modelings, the reaction sphere geometry is simplified in Fig. 2 with parameters listed in Table I. The simplification includes two aspects. First, assembled stator back irons are modeled as a complete stator shell. The air domain (including stator windings) between the rotor and the stator is referred to as Region I. Region II and Region III are the copper layer and the steel core of the rotor, respectively. Second, currents carried by the three-phase full-pitch windings are approximated by surface

TABLE I
PARAMETERS OF THE REACTION SPHERE

Symbol	Value	Meaning
R_s	30 mm	Inner radius of the stator back iron
R_r	25 mm	External radius of the copper layer
R_b	20 mm	External radius of the steel core
ψ	65°	Stator windings are within $\theta \in [\psi, 180° - \psi]$
I_s	2 A	Input AC current magnitude
ω	20π rad/s	Input AC current angular frequency
N	270	Turn number per phase per pole
p	1	Pole-pair number
k_w	0.96	Fundamental distribution factor of phase windings
$\mu_{r,c}$	$0.999994 \approx 1$	Relative permeability of Region II
μ_r	30	Relative permeability of Region III
$\mu_{r,iron}$	4000	Relative permeability of stator back iron
σ	$5.998{\times}10^7$ S/m	Electrical conductivity of Region II
σ_{III}	$4.02{\times}10^6$ S/m	Electrical conductivity of Region III
σ_{iron}	$1.12{\times}10^6$ S/m	Electrical conductivity of stator back iron

currents. For convenience, the field modeling is conducted in a spherical frame, which is attached to the stator and presented in Fig. 2. The approximated surface currents with the density of $J_s \cos(\omega t - \phi)/\sin\theta \cdot \vec{e}_\theta$ are distributed at $r = R_s$ within $\theta \in [\psi, \pi - \psi]$. The sign of J_s is determined by the direction of energized currents and its magnitude is $|J_s| = 3k_w N I_s/(\pi R_s)$ [16].

Assumptions employed in the field modeling are as follows.

1) The stator back iron is slotless, without openings.
2) Relative permeability of the stator back iron is infinite.
3) No iron saturation.
4) Input stator currents are sinusoidal.
5) High-order space harmonics caused by nonsinusoidal winding distributions are neglected.
6) The study is only for sinusoidal steady states.

The flux density distribution within the actuator is solved by introducing the magnetic vector potential $\vec{A}$ and converting Maxwell's equations to governing equations for each domain. Since stator windings are modeled as surface currents, Region I and Region III are governed by Laplace's Equations. When the rotor is stationary (i.e., the slip $s = 1$), Region II is governed by a heat diffusion equation, due to eddy currents induced in the copper area

$$\nabla^2 \vec{A}_i = 0 \quad (\mathrm{i = I, III}) \tag{1a}$$

$$\nabla^2 \vec{A}_{II} = \mu_0 \mu_{r,c} \sigma \frac{\partial \vec{A}_{II}}{\partial t} \tag{1b}$$

where μ_0 is the permeability of vacuum, and $\mu_{r,c}$ and σ are the relative permeability and the electrical conductivity of copper, respectively.

Equations (1a) and (1b) are solved through the analytical approach presented in [16]. The distribution of magnetic flux density $\vec{B}$ is obtained through $\vec{B} = \nabla \times \vec{A}$. Resultant distributions of $B_{II,r}$ and $B_{II,\phi}$ in Region II are

$$B_{II,r}(r,\theta,\phi) = -2\sum_{n=1}^{\infty} Re\left[\left(\kappa_n i_n(ar) + \eta_n k_n(ar)\right)\frac{n(n+1)}{r} Q_n^1(\theta) e^{j(\omega t - \phi)}\right] \tag{2a}$$

$$B_{II,\phi}(r,\theta,\phi) = 2\sum_{n=1}^{\infty} Re\left[\left(\kappa_n X_n(ar) - \eta_n Y_n(ar)\right)\frac{jQ_n^1(\theta)}{r\sin\theta} e^{j(\omega t - \phi)}\right]. \tag{2b}$$

The complex coefficient a is defined as $a = \sqrt{j\omega\mu_0\mu_{r,c}\sigma}$. $i_n(ar)$ and $k_n(ar)$ are modified spherical Bessel functions. κ_n, η_n, $X_n(ar)$, $Y_n(ar)$, and $Q_n^1(\theta)$ are defined in the Appendix.

To validate the analytical field model, a FEM is developed in COMSOL. Input parameters of the numerical model are consistent with those listed in Table I. In Fig. 3, analytically calculated distributions of B_r and B_ϕ on the curve ($r = R_r$, $\theta = \pi/2$ and $\phi \in [0, 2\pi]$) at the time instant $t = 0.1$ s are illustrated and compared to numerical results obtained from the FEM. Deviations are caused by space harmonics in winding distributions and eddy currents induced in the stator back iron in the numerical model.

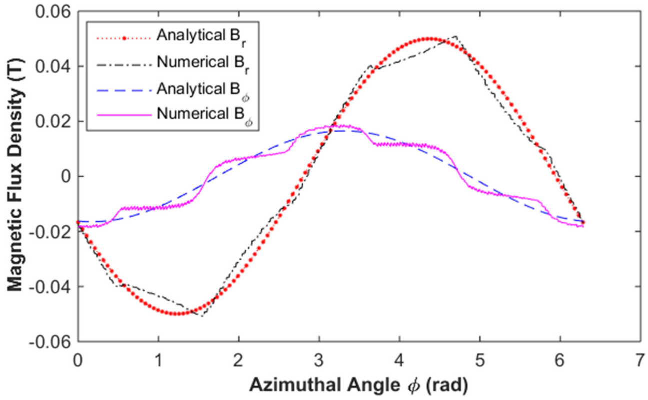

Fig. 3. Distributions of B_r and B_ϕ on the curve ($r = R_r$, $\theta = \pi/2$, and $\phi \in [0, 2\pi]$).

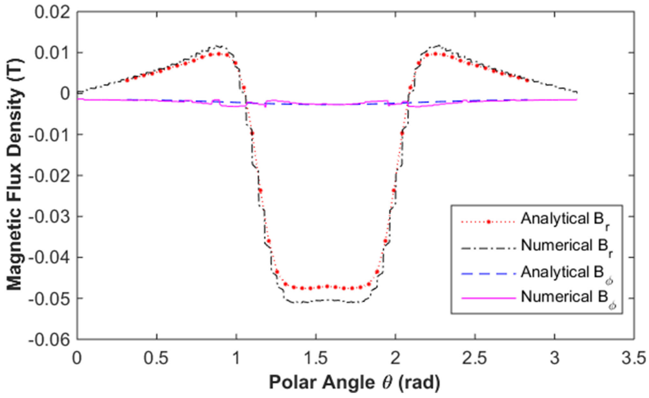

Fig. 4. Distributions of B_r and B_ϕ on the curve ($r = R_r$, $\theta \in [0, \pi]$, and $\phi = \pi/2$).

In Fig. 4, analytical and numerical results of B_r and B_ϕ distributions on the curve ($r = R_r$, $\theta \in [0, \pi]$, and $\phi = \pi/2$) at the time instant $t = 0.1$ s are compared. Deviations presented at the equatorial area (where θ is close to $\pi/2$) correspond to discrepancies illustrated in Fig. 3 and they are caused by space harmonics. Differences in the B_r distribution at the transverse edge region (where $\theta \approx 0.9$ and $\theta \approx 2.2$) are caused by the transverse end effect.

In fact, the analytical model in [16] also allows the calculation of magnetic flux density distribution at $s = 0$. In that case, the governing equation of Region II degrades to a Laplace equation since no eddy currents are induced. All the boundary conditions keep unchanged.

Additionally, the analytical field model can be extended to take high-order space harmonics into account. This is done by replacing $\cos(\omega t - \phi)$ in the formula of the approximated surface current density with Fourier series, which are obtained from the Fourier expansion of the three-phase winding distribution function. Although the extended field model describes the flux density distribution in the numerical model better, the model without high-order harmonics is adopted here, for two reasons. First, compared to the fundamental element, high-order harmonics contribute little to the overall performance of the actuator [17]. Second, in Section III, performances of the single-axis spinning reaction sphere are predicted through the equivalent circuit approach. The determination and validation of circuit parameters corresponding to high-order space harmonics are challenging. Therefore, high-order space harmonics are not considered.

III. PARAMETER DETERMINATION

Based on the solved magnetic flux density distribution, electromagnetic torques acting on the rotor can be calculated through Maxwell stress tensor [16]

$$T_{\mathrm{MST}} = \int_0^{2\pi} \int_0^{\pi} H_\phi B_r r^3 \sin^2\theta \, \mathrm{d}\theta \mathrm{d}\phi. \tag{3}$$

However, the field model in Section II is only for cases of blocked-rotor ($s = 1$) or synchronous rotations ($s = 0$). If the reaction sphere is spinning at a velocity $\vec{v}$ (a nonsynchronous speed), the governing equation of Region II will become [18]

$$\nabla^2 \vec{A} = \mu_0 \mu_{r,c} \sigma \left(\frac{\partial \vec{A}}{\partial t} - \vec{v} \times (\nabla \times \vec{A}) \right). \tag{4}$$

Since the magnetic vector potential $\vec{A}$ has three components, the vector $\vec{v} \times (\nabla \times \vec{A})$ is not necessarily aligned with the vector $\partial\vec{A}/\partial t = j\omega\vec{A}$. From the mathematical aspect, it does not make sense to simplify $\partial\vec{A}/\partial t - \vec{v} \times (\nabla \times \vec{A})$ to $j(\omega - \omega_m)\vec{A}$ where $\omega_m = v/r$ is the mechanical angular speed. The formula $\partial\vec{A}/\partial t - \vec{v} \times (\nabla \times \vec{A})$ involves many items. Without specific values, it is difficult to determine which item is significant and which item is negligible from the mathematical aspect. Therefore, simplifying (4) and calculating driving torques at a random slip through the analytical way is difficult.

Due to the resemblance between the single-axis rotating reaction sphere and conventional induction machines, the equivalent circuit approach is adopted to predict generated torques.

Typically, parameters involved in the equivalent circuit are derived from the no-load ($s = 0$) and blocked-rotor ($s = 1$) experiments with the assumption of identical inductances of the stator leakage $L_{s\sigma}$ and referred rotor leakage $L'_{R\sigma}$ [19]. However, due to toroidal windings, $L_{s\sigma}$ is expected to be much larger than $L'_{R\sigma}$ and the typical method becomes inapplicable. To help researchers determine circuit parameters of a newly designed reaction sphere quickly, an analytical way is presented here.

A. Parameter Determination Based on the Field Model

To facilitate the calculation of a flux linkage, we assume that the copper layer on the rotor is replaced by short-circuit windings. In this article, high-order space harmonics are neglected in both the stator and rotor winding distributions. The flux linkage of rotor windings is calculated by [20] (with the magnitude-invariant Clarke transformation)

$$|\vec{\lambda}_r^s| = \lambda_{rp} = N_{re} \cdot \Phi_{rp} \cdot \pi/4. \tag{5}$$

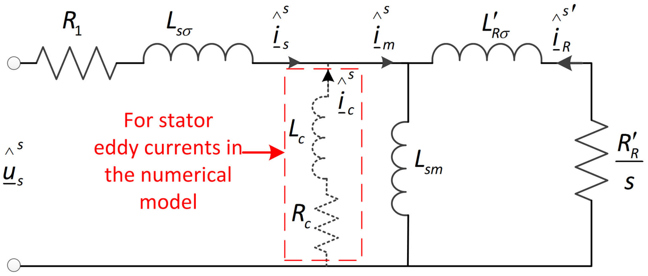

Fig. 5. Equivalent circuit of induction machines for the steady state.

The superscript s refers to the stator frame. Φ_{rp} is the maximum flux per pole flowing through rotor windings and N_{re} is the effective turn number per phase per pole, corresponding to the fundamental element in the winding distribution. Since rotor windings are virtual, N_{re} is unknown. However, when $\vec{\lambda}_r^s$ is referred to the stator side by $\vec{\lambda}_R^{s\prime} = (N_{se}/N_{re})\vec{\lambda}_r^s$ [20], the referred rotor flux linkage becomes $|\vec{\lambda}_R^{s\prime}| = N_{se}\Phi_{rp}\pi/4$. N_{se} is the effective turn number of stator windings and is calculated by $N_{se} = 4k_w N/\pi$. Hence, the referred rotor flux linkage becomes $|\vec{\lambda}_R^{s\prime}| = k_w N \Phi_{rp}$.

Given the filed distribution, Φ_{rp} can be obtained by integrating B_r on the surface at $r = R_w$ (the radial center of rotor windings or eddy currents). However, due to the skin effect, to determine the location of $r = R_w$ is challenging. Therefore, B_r is integrated on the external and internal surfaces of Region II, respectively, and the average is taken: $\Phi_{rp} = (\Phi_{rp,Rb} + \Phi_{rp,Rr})/2$. Since azimuthal currents (flowing along $\vec{e}_\phi$) are induced on the rotor, integrations of B_r are executed within specific ranges of θ. The center of azimuthal eddy currents is assumed to be parallel to the center of stator end windings (see Fig. 2, at the height $z^* = R_s \cos\psi$). Therefore, integration ranges are $\theta \in [\theta_b, \pi - \theta_b]$ (where $\theta_b = \cos^{-1}(z^*/R_b)$) on the surface at $r = R_b$ and $\theta \in [\theta_r, \pi - \theta_r]$ (where $\theta_r = \cos^{-1}(z^*/R_r)$) at $r = R_r$, respectively:

$$\Phi_{rp,R_b} = \int_{\phi_b}^{\phi_b+\pi} \int_{\theta_b}^{\pi-\theta_b} B_r(R_b, \theta, \phi) R_b^2 \sin\theta \, \mathrm{d}\theta \, \mathrm{d}\phi \tag{6a}$$

$$\Phi_{rp,R_r} = \int_{\phi_r}^{\phi_r+\pi} \int_{\theta_r}^{\pi-\theta_r} B_r(R_r, \theta, \phi) R_r^2 \sin\theta \, \mathrm{d}\theta \, \mathrm{d}\phi. \tag{6b}$$

ϕ_b and ϕ_r are angles which make Φ_{rp,R_b} and Φ_{rp,R_r} achieve their maximum.

Meanwhile, the expression of $\vec{\lambda}_R^{s\prime}$ in the equivalent circuit (see Fig. 5) is

$$\vec{\lambda}_R^{s\prime} = L'_{R\sigma}\vec{i}_R^{s\prime} + L_{sm}\left(\vec{i}_s^s + \vec{i}_R^{s\prime}\right) \tag{7}$$

where L_{sm} is the magnetization inductance, and $\vec{i}_s^s$ and $\vec{i}_R^{s\prime}$ are vectors of the stator current and the referred rotor current, respectively.

In steady states of $s = 0$, there are no rotor currents. With the known stator current, L_{sm} can be calculated through

$$L_{sm} = \left| \frac{\hat{\underline{\lambda}}_{R,s=0}^{s\prime}}{\hat{\underline{i}}_{s,s=0}^{s}} \right| = \frac{k_w N \Phi_{rp,s=0}}{|\hat{\underline{i}}_{s,s=0}^{s}|}. \tag{8}$$

TABLE II
PARAMETER DETERMINATION BASED ON THE FIELD DISTRIBUTION

	Param	Analytical model	Numerical model
$s=0$	$\lvert\underline{\hat{i}}^{s}_{s,s=0}\rvert$	2 A	2 A
	$\lvert\underline{\hat{i}}^{s}_{c,s=0}\rvert$	0 A	0.0238 A (α=π-1.45)
	$\lvert\underline{\hat{\lambda}}^{s\prime}_{R,s=0}\rvert$	$k_w N \cdot 5.635 \times 10^{-5}$ Wb	$k_w N \cdot 5.628 \times 10^{-5}$ Wb
$s=1$	$\lvert\underline{\hat{i}}^{s}_{s,s=1}\rvert$	2 A	2 A
	$\lvert\underline{\hat{i}}^{s}_{c,s=1}\rvert$	0 A	0.0226 A (α=π-1.45)
	$\lvert\underline{\hat{\lambda}}^{s\prime}_{R,s=1}\rvert$	$k_w N \cdot 4.83 \times 10^{-5}$ Wb	$k_w N \cdot 4.75 \times 10^{-5}$ Wb
	$T_{s=1}$	12.18 mNm	12.16 mNm
Outputs	L_{sm}	7.30 mH	7.29 mH
	$L'_{R\sigma}$	4.29 mH	4.53 mH
	R'_R	1.214 Ω	1.175 Ω

Symbols with a hat refer to variables in steady states and phasors (complex quantities) are underlined.

In the steady state of $s=1$, the electromagnetic torque is [17], [19]

$$T_{s=1} = 1.5 R'_R |\underline{\hat{i}}^{s\prime}_{R,s=1}|^2/\omega \tag{9}$$

where R'_R is the referred rotor resistance. With solved magnetic flux density distribution, $T_{s=1}$ can be obtained by the Maxwell stress tensor. Additionally, the rotor voltage equation in steady states is

$$0 = R'_R \underline{\hat{i}}^{s\prime}_R/s + j\omega\underline{\hat{\lambda}}^{s\prime}_R. \tag{10}$$

With the known ω, analytically calculated $T_{s=1}$ and $|\underline{\hat{\lambda}}^{s\prime}_{R,s=1}|$, the magnitude of $\underline{\hat{i}}^{s\prime}_{R,s=1}$ and R'_R can be solved through the equation set of (9) and (10).

As per (10), $\underline{\hat{i}}^{s\prime}_R$ is orthogonal to $\underline{\hat{\lambda}}^{s\prime}_R$ in the phasor diagram. Based on this relation and the Pythagorean theorem, $L'_{R\sigma}$ can be calculated by transforming (7) to

$$L'_{R\sigma} = \sqrt{L^2_{sm}|\underline{\hat{i}}^{s}_{s,s=1}|^2 - |\underline{\hat{\lambda}}^{s\prime}_{R,s=1}|^2} \Big/ |\underline{\hat{i}}^{s\prime}_{R,s=1}| - L_{sm}. \tag{11}$$

Related data and derived parameters are listed in Table II. Since the actuator will be fed with controlled stator currents, only L_{sm}, $L'_{R\sigma}$, and R'_R are concerned in the equivalent circuit.

For comparison, the presented determination method is applied to the numerical model developed in COMSOL. Φ_{rp,R_b} and Φ_{rp,R_r} in (6) are obtained by integration of the local B_r distribution on the internal and external surfaces of Region II in the numerical model. Referred rotor flux linkages $|\underline{\hat{\lambda}}^{s\prime}_{R,s=0}|$ and $|\underline{\hat{\lambda}}^{s\prime}_{R,s=1}|$ are obtained through $|\underline{\hat{\lambda}}^{s\prime}_R| = 0.5k_w N(\Phi_{rp,R_b} + \Phi_{rp,R_r})$ in no-load and blocked-rotor simulations, respectively. The torque $T_{s=1}$ is provided by the Maxwell Stress Tensor feature in the blocked-rotor simulation.

In the numerical model, since eddy currents are induced in the stator back iron, the current virtually flowing to the airgap and the rotor side in the equivalent circuit becomes $\underline{\hat{i}}^{s}_m$ (see Fig. 5 where the resistance R_c and inductance L_c of the stator iron are included). The stator eddy current $\underline{\hat{i}}^{s}_c$ is identified from the numerical model by two steps. First, integrating the volume density of stator eddy currents on the equatorial plane within per pole area results in I_{is}. Next, stator eddy currents are approximated as sinusoidally distributed surface currents at $r = R_s+\delta$ (where δ is very small). The magnitude of approximated surface current density is $J_{is}/\sin\theta \approx (I_{is}/2R_s)/\sin\theta$. Due to the high permeability of the stator iron, the distribution of H_ϕ at $r = R_{s+}$ (the side within the stator iron, i.e., $R_{s+} > R_s$) is analyzed through the image method which results in $H_\phi|_{r=R_{s+}} \approx 2J_{is}\cos(\omega t + \alpha - \phi)/\sin\theta$. The angle α is the phase difference between distributions of stator eddy current density and input stator current density on the equatorial plane. To reveal the influence of stator eddy currents, the boundary condition at $r = R_s$ in the analytical field model is recalled. Due to J_{is}, it becomes

$$H_{I\phi}|_{r=R_s} = \frac{J_s}{\sin\theta}\cos(\omega t - \phi) + \frac{2J_{is}}{\sin\theta}\cos(\omega t + \alpha - \phi). \tag{12}$$

Inverting the calculation of J_s from $|\underline{\hat{i}}^{s}_s|$, $|\underline{\hat{i}}^{s}_c|$ is obtained from $2J_{is}$. The phase angle is $\arg\underline{\hat{i}}^{s}_c = \arg\underline{\hat{i}}^{s}_s + \alpha$.

With known input stator currents and quantified stator eddy currents for both the no-load and the blocked-rotor simulations, obtained $|\underline{\hat{\lambda}}^{s\prime}_{R,s=0}|$, $|\underline{\hat{\lambda}}^{s\prime}_{R,s=1}|$ and $T_{s=1}$, circuit parameters (i.e., L_{sm}, $L'_{R\sigma}$ and R'_R) corresponding to the numerical field model are derived from (8)–(11).

As illustrated in Table II, differences between circuit parameters derived from the analytical field model and those derived from the numerical field model are within 6%.

B. Partial Validation of the Proposed Parameter Determination Method

In this section, the no-load and blocked-rotor method is applied with the assumption of $L_{sm} = 7.3$ mH, to partially validate parameters determined in Section III-A. Since prototypes are not available, required electrical measurements are obtained from dynamic simulations of the 3-D numerical model. The numerical model is built in COMSOL through the rotating machinery, magnetic physics interface. It is the same numerical model, which has been mentioned in Section II and Section III-A. Electrical data such the stator current, resistance, and voltage of each winding phase, as well as the three-phase power are available. Simulations for the case of no-load and the case of blocked-rotor were run respectively. Electrical measurements obtained from the dynamic simulations are listed in Table III.

In the numerical model, since stator windings are nonsinusoidally distributed, space harmonics exist. The extended equivalent circuit considering space harmonics [21], [22] is presented in Fig. 6. Except for parameters corresponding to the fundamental space harmonic (i.e., R_c, L_{sm}, R'_R, and $L'_{R\sigma}$), circuit parameters corresponding to high-order harmonics are also involved. Compared to Fig. 5, L_c is missing in Fig. 6. The reason is explained later in this section. Since the purpose of this section is to validate circuit parameters derived in Section III-A, which are for the fundamental harmonic, only L_{sm}, R'_R, and $L'_{R\sigma}$ are concerned here. Due to the difficulty of determining all involved parameters, circuits corresponding to high-order harmonics are transformed to an equivalent serial circuit composed of R_{add} and L_{add} in Fig. 6. Values of R_{add} and L_{add} vary with input frequencies and the slip.

TABLE III
PARAMETER DETERMINATION BASED ON ELECTRICAL DATA

	Parameters	No-load	Blocked-rotor
Measurements	Stator resistance	R_1 =2.335Ω	R_1 = 2.335 Ω
	Phase current	I_{NL}=$\sqrt{2}$ A (rms)	I_{BL}=$\sqrt{2}$ A (rms)
	Phase voltage	U_{NL}= 3.05$\sqrt{2}$ V (rms)	U_{NL}= 3.1$\sqrt{2}$ V (rms)
	3-phase power	P_{NL}=14.1 W	P_{BL}=14.9 W
	Stator eddy current	$I_{c,NL}$= 0.0238/$\sqrt{2}$ A (rms)	$I_{c,BL}$= 0.0226/$\sqrt{2}$ A (rms)
	Output torque		T_{BL}=12.16 mNm
Assumption	$L_{sm} = 7.30$ mH		
Outputs	$L_{s\sigma} + L_{add} = 23.64$ mH		
	$L'_{R\sigma} = 4.675$ mH		
	$R'_R = 1.127$ Ω		

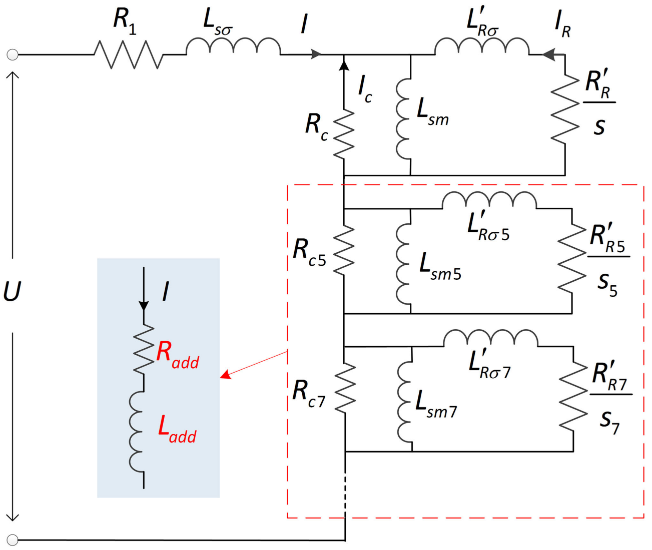

Fig. 6. Extended equivalent circuit for the numerical model.

As mentioned at the beginning of this section, the partial validation is conducted with the assumption of $L_{sm} = 7.3$ mH. R'_R and $L'_{R\sigma}$ derived from the electrical measurements will be compared to those listed in Table II.

Although R_1 is directly available from COMSOL simulations and L_{sm} is assumed, it is still difficult to determine rest of the parameters in the transformed equivalent circuit. In the conventional electrical measurement approach, measured phase voltages, phase currents, and three-phase powers result in four equations in total.

1) When the rotor is running at $s = 0$ (no-load) with the input angular frequency of ω

$$R_1 + R_{\text{add},NL} + R_{NL} = \frac{P_{NL}}{3I_{NL}^2} \tag{13a}$$

$$X_{s\sigma} + X_{\text{add},NL} + X_{NL} = \sqrt{\left(\frac{V_{NL}}{I_{NL}}\right)^2 - \left(\frac{P_{NL}}{3I_{NL}^2}\right)^2}. \tag{13b}$$

where $Z_{NL} = R_{NL} + jX_{NL}$ is the impedance of the parallel circuit formed by R_c and $j\omega L_{sm}$ in the no-load state. Since all space harmonics have the same angular frequency ω [23], the reactance X is always the product of ω and the corresponding inductance L.

2) When the rotor is running at $s = 1$ (blocked-rotor) with the input angular frequency of ω

$$R_1 + R_{\text{add},BL} + R_{BL} = \frac{P_{BL}}{3I_{BL}^2} \tag{14a}$$

$$X_{s\sigma} + X_{\text{add},BL} + X_{BL} = \sqrt{\left(\frac{V_{BL}}{I_{BL}}\right)^2 - \left(\frac{P_{BL}}{3I_{BL}^2}\right)^2} \tag{14b}$$

where $Z_{BL} = R_{BL} + jX_{BL}$ is the impedance of the parallel circuit formed by R_c, $j\omega L_{sm}$, and $R'_R + j\omega L'_{R\sigma}$ in the blocked-rotor simulation.

However, the number of unknowns in above equations is more than 4. Therefore, to derive the values of R'_R and $L'_{R\sigma}$, some simplifications are required.

1) As illustrated in Fig. 6, powers are consumed on R_1, R_c, R'_R, and R_{add}. In the case of no-load simulation, due to the unknown R_{add}, there is no way to determine R_c from the power aspect. As $I_{c,NL}$ can be measured from the numerical simulation (see the end of Section III-A) and the stator current $I_{NL} = \sqrt{2}$ A is known, R_c can be determined from

$$\left|\frac{j\omega L_{sm}}{R_c + j\omega L_{sm}}\right| \cdot I_{NL} = I_{c,NL}. \tag{15}$$

Theoretically, both R_c and L_c (as well as R_{cv} and L_{cv}) shall be included in the equivalent circuit (see Fig. 5). However, the determination of L_c requires additional information. For instance, with the phase difference α between $I_{c,NL}$ and I_{NL} (corresponding to the phase difference between $\hat{\underline{i}}^s_{c,s=0}$ and $\hat{\underline{i}}^s_{s,s=0}$ in Fig. 5) measured from the numerical model, L_c and R_c can be determined from

$$\frac{j\omega L_{sm}}{R_c + j\omega L_c + j\omega L_{sm}} = \frac{I_{c,NL}}{I_{NL}} e^{i(\pi-\alpha)}. \tag{16}$$

Since both R_c and L_c are unknown, their solutions derived from (16) are very sensitive to α, which, however, cannot be measured accurately in the numerical model. Therefore, the conventional engineering strategy is adopted here to neglect L_c and treat the impedance $R_c + j\omega L_c$ as purely active resistance [21]. That is why L_c and L_{cv} are missing in Fig. 6.

2) Slips corresponding to the vth ($v = 5, 7, 11...$) space harmonic is $s_v = (1 - v) + v \cdot s$ (if the harmonic is forward rotating) or $s_v = (1 + v) - v \cdot s$ (if the harmonic is backward rotating) [21]. In the case of $s = 0$, s_5 and s_7 are 6 and −6, respectively. At $s = 1$, all the slips equal to 1. In the no-load or blocked-rotor simulation, depending on s_v, the value of X_{add} varies. However, at a specific ω, the variation of X_{add} with s_v is negligible and $X_{s\sigma} + X_{\text{add}}$ can be assumed constant. This simplification is based on the following consideration. As per [21], $L'_{R\sigma v}$ is close

to $L'_{R\sigma}$ and R'_{Rv} is close to R'_R. Meanwhile, the magnetizing reactance X_{smv} (or the differential leakage inductance $L_{smv} = X_{smv}/\omega$) is proportional to $(k_{wv}/v)^2$ [21], where k_{wv} is the winding factor for the vth harmonic. For the employed distributed full-pitch windings, $\max\{k_{wv}\}$ is around 0.2 and much smaller than the fundamental k_w. Therefore, the maximum L_{smv} (occurring at $v = 5$) is about $L_{sm}/100$. As per values derived in Table II, $L'_{R\sigma v}$ is much larger than L_{smv}. Therefore, the value of X_{add} changes very slightly with s_v.

With R_c determined from (15) and L_{sm} assumed, $X_{s\sigma} + X_{\text{add},BL} = X_{s\sigma} + X_{\text{add},NL}$ can be determined from (13b). Replacing it into (14b), X_{BL} is obtained.

3) Since R_{cv} is unknown, the value of $R_{\text{add},BL}$ may be quite different from that of $R_{\text{add},NL}$. Therefore, the determination of R_{BL} in (14a) requires additional information. At $s = 1$, the three-phase copper loss on the rotor ($3I_{R,BL}^2 R'_R$) equals to $T_{BL} \cdot \omega$ [17] where ω is known and T_{BL} is available in the numerical simulation. Besides, the three-phase copper loss on the stator iron is $3I_{c,BL}^2 R_c$, where R_c is determined from (15) and $I_{c,BL}$ is obtained from the numerical model. Hence, (14a) can be transformed to

$$\begin{aligned} 3(R_1 + R_{BL})I_{BL}^2 &= P_{BL} - 3R_{\text{add}}I_{BL}^2 \\ &= T_{BL} \cdot \omega + 3R_1 I_{BL}^2 + 3R_c I_{c,BL}^2 \end{aligned} \tag{17}$$

and R_{BL}, therefore, can be obtained.

Since the obtained $R_{BL} + jX_{BL}$ is the impedance of the parallel circuit formed by $R_c + j\omega L_c$, $j\omega L_{sm}$ and $R'_R + j\omega L'_{R\sigma}$, rotor quantities (i.e., R'_R and $L'_{R\sigma}$) can be easily calculated. Parameters derived in the last column of Table II and those in Table III are based on the same numerical model. Their difference in R'_R is about 4.1% and the difference in $L'_{R\sigma}$ is about 3.2%.

Above, rotor quantities are determined from the state of $s = 1$, where the (electrical) slip angular frequency $\Delta\omega = s \cdot \omega$ equals to ω. To check variations of determined circuit parameters with $\Delta\omega$, both the field distribution-based and the electrical measurement-based methods are implemented with a series of input frequencies. Since L_{sm} is identified from $|\hat{\underline{\lambda}}^{s\prime}_{R,s=0}|$, which is independent of ω, it keeps constant. Variations of R'_R and $L'_{R\sigma}$ are illustrated in Fig. 7. In the electrical measurement-based methods, L_{sm} is always assumed to be 7.3 mH [24]. Since L_{add} depends on the input angular frequency ω, $L_{s\sigma} + L_{\text{add}}$ applied to each block-rotor simulation shall be obtained from their corresponding no-load simulations. It is interesting to note that R_c obtained from each no-load simulation also varies with the input ω. This variation is due to the neglected L_c.

In Fig. 7, the increase of R'_R and the decrease of $L'_{R\sigma}$ are caused by the skin effect [24]. Instead of evenly distributed in the cross section of Region II, eddy currents tend to concentrate in the upper layer when the slip frequency increases. The nonuniform distribution of eddy currents results in the increase of R'_R. Meanwhile, compared to currents flowing in the bottom layer, currents distributed in the upper layer link with less leakage flux, which means a low leakage inductance. Therefore, $L'_{R\sigma}$ decreases when the slip frequency increases.

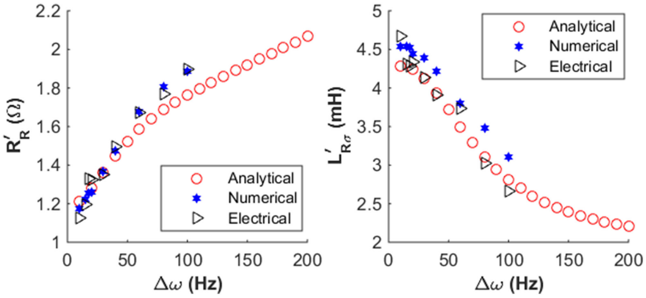

Fig. 7. R'_R and $L'_{R\sigma}$ determined through the analytical/numerical field models and electrical measurements.

In Fig. 7, deviations between parameters derived from the analytical/numerical field models and those derived from electrical measurements are mainly caused by the neglected L_c and the resultantly overestimated R_c, as well as measurement errors. As illustrated in Fig. 5, L_c exists and connects serially to R_c. In the no-load simulation, when ω increase, more currents will flow through R_c since the reactance $X_{sm} = \omega L_{sm}$ increases. However, due to the existence of L_c, the increase of $I_{c,NL}$ is not as large as expected. Therefore, R_c derived from (15) is larger than its actual value. As per (17), the overestimated R_c leads to an overestimated R_{BL}. As a result, R'_R derived from the overestimated R_{BL} is slightly larger than its actual value while $L'_{R\sigma}$ is slightly smaller than its actual value. Hence, R'_R derived from electrical measurements increases faster while $L'_{R\sigma}$ decreases faster than those derived from the analytical/numerical field models. Their deviations become larger at high slip frequencies.

C. Steady-State Torque–Speed Curve

If there are no stator eddy currents, output torques of the reaction sphere (with the pole-pair number $p = 1$) in steady states can be expressed as

$$T = \frac{3}{2}\frac{R'_R|\hat{\underline{i}}^{s\prime}_R|^2}{s \cdot \omega} = \frac{1.5L_{sm}^2|\hat{\underline{i}}^{s}_s|^2 R'_R/\Delta\omega}{(R'_R/\Delta\omega)^2 + (L'_{R\sigma} + L_{sm})^2}. \tag{18}$$

As illustrated by (18), torques generated by the current-controlled induction machine depend on the slip angular frequency $\Delta\omega$ rather than the input angular frequency or the mechanical speed. Applying circuit parameters derived in the third column of Table II and the controlled input $|\hat{\underline{i}}^{s}_s| = 2$ A to (18) results in the steady-state torque–speed curve (the solid line) in Fig. 8. This curve predicts how much driving torques are generated when the actuator is running at different slip frequencies.

To check the prediction accuracy, steady-state torque–speed curves obtained from the analytical field model and numerical simulations are presented in Fig. 8 too. First, due to the relation of $\Delta\omega = s \cdot \omega$, the value of $\Delta\omega$ can be adjusted by varying the slip s or the input angular frequency ω. Since torques at $s = 1$ can be calculated through the analytical field model directly, applying the fixed $s = 1$ and various ω to (3) results in a series of analytically calculated $T_{s=1}$ in Fig. 8. In numerical simulations, the same strategy (fixed $s = 1$ and varying ω) is adopted. This

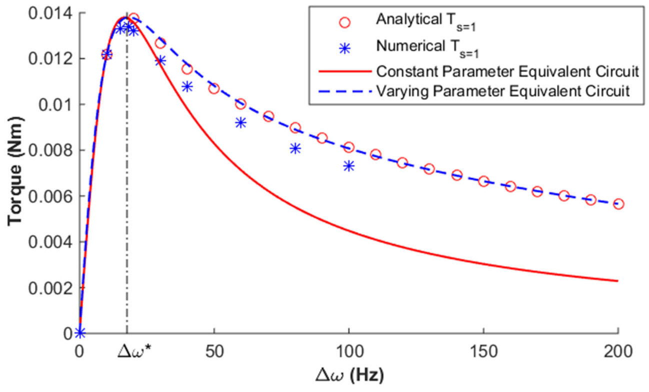

Fig. 8. Steady-state torque–speed curve of the single axis rotation.

is because the spinning rotor in COMSOL is modeled through moving mesh which makes time-dependent simulations even slower. Therefore, the numerical $T_{s=1}$ dataset is obtained from simulations with various input frequencies and it is shown in Fig. 8 too.

Second, for an induction motor, its stable operation region is $\Delta\omega \in [0, \Delta\omega^*]$. $\Delta\omega^*$ corresponds to the slip frequency where the maximum torque T^* occurs. When the equivalent circuit model is employed for torque prediction, its prediction accuracy within the stable operation region is more concerned rather than outside the region. As illustrated in Fig. 8, deviations between torques predicted from the equivalent circuit model [i.e., through (18)] and those obtained from (3) or numerical simulations become larger when $\Delta\omega$ increases. Within the stable operation region, maximum deviations occur at $\Delta\omega^*$. At this point, the torque (i.e., T^*) predicted from the equivalent circuit model deviates from the analytical and numerical $T_{s=1}$ by only 0.3% and 3%, respectively.

Differences between the analytically calculated $T_{s=1}$ and those from numerical simulations are mainly due to stator eddy currents in the numerical model. Although high-order space harmonics affect the numerical $T_{s=1}$ too, their influences at $s = 1$ are negligible [17]. At the end of Section III-A, the magnitude of induced stator eddy currents is quantified. If that part is subtracted from the stator input current in the analytical model, the resultant analytical $T_{s=1}$ would match the numerical $T_{s=1}$ well. In conventional induction machines, stator eddy currents can be suppressed by employing laminated steel. However, in the spherical machine, to ensure the high permeability of magnetic paths along with multiple directions, it is challenging to suppress unwanted eddy currents.

Deviations between the analytical $T_{s=1}$ curve and the torque–speed curve predicted by the equivalent circuit are caused by the varying R'_R and $L'_{R\sigma}$. To illustrate the influence, variations of R'_R and $L'_{R\sigma}$ are approximated by curve fitting. Applying $L_{sm} = 7.3$ mH, curve fitted R'_R and $L'_{R\sigma}$ to (18) results in the dashed line in Fig. 8, which fits the analytical $T_{s=1}$ curve well.

As presented above, the equivalent circuit model with constant circuit parameters predicts the achievable maximum torque T^* with reasonable accuracy. Based on (18), the achievable maximum torque of the reaction sphere occurs at

$$\Delta\omega^* = R'_R/(L_{sm} + L'_{R\sigma}) \tag{19}$$

and its value is

$$T^* = 0.75 L_{sm}^2 |\hat{\underline{i}}_R^{s\prime}|^2/(L_{sm} + L'_{R\sigma}). \tag{20}$$

In the proposed determination method, L_{sm}, R'_R, and $L'_{R\sigma}$ are obtained through the magnetic flux density distribution within the actuator, which is an analytical function of design variables. In this way, these circuit parameters can be expressed as analytical functions of design variables of the reaction sphere, too. Applying them to (19) and (20), optimizations regarding the achievable maximum torque or $\Delta\omega^*$ can be conducted quickly and easily.

IV. EXPERIMENTAL VALIDATION

As mentioned at the beginning of Section II, the studied reaction sphere is a basic design. Its performance analysis method, including the field modeling and circuit parameter determination, is generally applicable to induction-based spherical actuators. Below, the developed performance analysis method is validated through an experimental case presented in [25]. In that case, a spherical conductive rotor is driven by a pair of inductors to perform single-axis rotations. A single inductor is with six slots, spanning 60° along $\vec{e}_\phi$ and 35° along $\vec{e}_\theta$. With slots handled by the Carter factor [26] and end effects neglected, the two inductors are approximated as one-third of a complete six-pole-pair three-phase slotless winding set. The distribution of generated magnetic flux is solved by the analytical model presented in Section II. Due to the equivalent pole-pair number $p_e = 6$ of the complete winding set, the approximated stator surface current density changes to $J_s \cos(\omega t - 6\phi)/\sin\theta$.

Equivalent circuit parameters are determined based on the flux density distribution at $s = 0$ and $s = 1$ with the input frequency of 25 Hz. Torques generated by the inductors are calculated through (18) multiplied by the factual pole-pair number $p = 2$. Given the specific input stator current $|\hat{\underline{i}}_s^s|$ ($1.6 \times \sqrt{2}$ A [25]), steady-state torque–speed curves of the actuator can be predicted. In [25], torque measurements were conducted for two scenarios, where the rotor conductive layer is copper (W.Nr.2.0090 [27]) or the Cu-Zn-Sn alloy (W.Nr.2.0532). In both experimental scenarios, the rotor core is made of St-37 steel (SAE 1013), which has a high relative permeability ($\mu_r = 2000$). Equivalent circuit parameters determined through the proposed method for the copper rotor and the ally rotor are listed in Table IV.

Predicted and experimental torque–speed curves (with the input frequency of 25 Hz) are compared in Figs. 9 and 10. Their differences are mainly due to longitudinal end effects since transverse end effects have been taken into account by the analytically modeled eddy currents distribution.

Torques caused by longitudinal end effects are calculated by applying L_{sm}, R'_R, and $L'_{R\sigma}$ to the linear inductor model developed in [28]. They are added to torques predicted from the equivalent circuit model, resulting in modified torque–speed curves, which are also illustrated in Figs. 9 and 10. In both

TABLE IV
EQUIVALENT CIRCUIT PARAMETERS FOR THE COPPER ROTOR AND THE ALLY ROTOR

	Param	Copper	Cu-Zn-Sn alloy
Inputs	σ	4.3×10^7 S/m	1.3×10^7 S/m
	R_s	51.1 mm (considering the Carter factor)	
	R_r	50 mm	
	R_b	49 mm	
	ψ	72.5°	
	μ_r	2000	
	k_w	0.955	
	f	25 Hz (electrical input frequency)	
	p_e	6 (equivalent pole-pair number)	
	p	2 (factual pole-pair number)	
	N	180 (per phase per pole)	
Outputs	L_{sm}	0.0490 H	0.0490 H
	R'_R	37.87 Ω	125.2 Ω
	$L'_{R\sigma}$	0.00621 H	0.00628 H

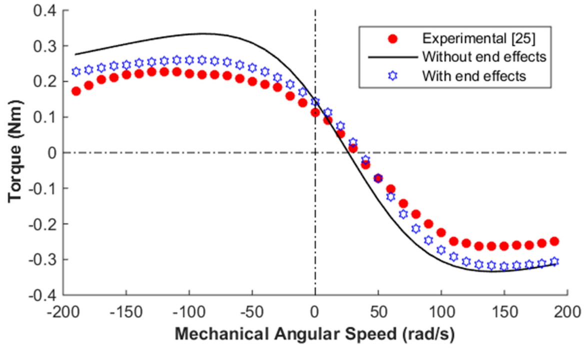

Fig. 9. Steady-state torque–speed curve of the copper rotor.

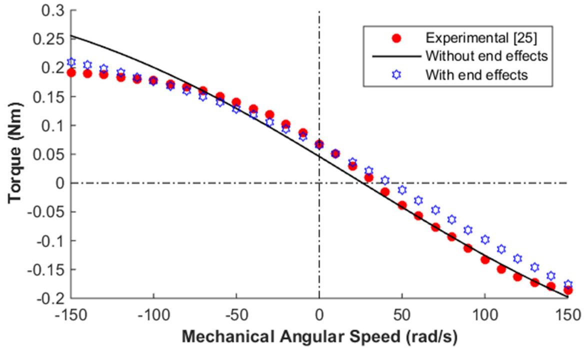

Fig. 10. Steady-state torque–speed curve of the Cu-Zn-Sn rotor.

figures, the mean absolute percentage error between the modified torque–speed curve (with end effects) and the corresponding experimental data is within 23%. Notable deviations in the generating mode are caused by simplifications in the modeling of entry and exit waves [28], which become invalid when the slip is negative. To the best of the author's knowledge, how to accurately model end effects is still a challenge in the field of linear and rotary inductors. For a specific design (with specific geometry parameters, supplied with a specific input frequency and running at a specific speed), the study of end effects can be conducted through FEM simulations. However, the torque generated by end effects changes with the input frequency and the rotor moving speed, as well as geometry parameters. Here, the end effect model presented in [28] is adopted for its acceptable accuracy.

Although the field model summarized in Section II and the circuit parameter determination method presented in Section III are for a basic case, they can be generally applied to a variety of induction-based spherical designs. For example, a different induction-based reaction sphere is described in [3]. Since its working principle is the same as the basic case presented in Section II, models and methods proposed in this article are applicable. Researchers just need to change the input parameters (such as geometry radii, and ψ which refers to the location of approximated stator surface currents) and will get the steady-state torque–speed curve of single-axis rotations in seconds. For more advanced scenarios such as the experimental case above, the developed basic models shall be extended by taking additional factors into account.

V. CONCLUSION

An induction-based reaction sphere was studied here. Performances of its single-axis rotation were analyzed through the equivalent circuit approach. Involved circuit parameters were determined through analytically solved magnetic field distributions. In this way, researchers can quickly evaluate the performances of newly designed actuators. Compared to numerical simulations and experiments on prototypes, the performance analysis method presented here gave results within minutes, saving time and cost greatly. Besides, it can be generally applied to spherical induction-based actuators. In cases where the rotor is driven by linear inductors rather than a complete winding set, the presented performance analysis is still applicable but end effects shall be considered.

When the rotor is driven by multiple sets of stator windings to perform rotations about an arbitrary axis, cross couplings are caused by kinematics. The direction of generated torques is not simply aligned with that of the revolving field or the spin axis of the rotor. Instead, the generated torques can be decoupled into components aligned with or perpendicular to the field revolving direction. Besides, the magnitude of each torque component is also affected by the coupling effect. Performances of rotations about an arbitrary axis will be presented in a future paper soon.

APPENDIX A

Here, functions involved in the article are defined

$$X(ar) = \frac{ar}{2n+1}\left[(n+1)i_{n-1}(ar) + n i_{n+1}(ar)\right] \tag{A.1}$$

$$Y(ar) = \frac{ar}{2n+1}\left[(n+1)k_{n-1}(ar) + n k_{n+1}(ar)\right] \tag{A.2}$$

$$Q_n^1(\theta) = \sqrt{\frac{2n+1}{4\pi}\frac{(n-1)!}{(n+1)!}}P_n^1(\cos\theta) \tag{A.3}$$

where $P_n^1(\cos\theta)$ is associated Legendre polynomial

$$\begin{aligned} H_n &= n(1+n)(1-s_2^{1+2n})\cdot \\ &\quad [\mu_r\,(k_n(as_2R_s)X_n(as_1R_s) + i_n(as_2R_s)Y_n(as_1R_s)) \\ &\quad + (1+n)\,(i_n(as_2R_s)k_n(as_1R_s) \\ &\quad - i_n(as_1R_s)k_n(as_2R_s))] \\ &\quad + (1+n+ns_2^{1+2n}) \\ &\quad [\mu_r\,(X_n(as_2R_s)Y_n(as_1R_s) - X_n(as_1R_s)Y_n(as_2R_s)) \\ &\quad + (1+n)\,(k_n(as_1R_s)X_n(as_2R_s) \\ &\quad + i_n(as_1R_s)Y_n(as_2R_s))] \end{aligned} \tag{A.4}$$

$$\kappa_n = \frac{(1+2n)s_2^n R_s N_n\,[(1+n)k_n(as_1R_s) + \mu_r Y_n(as_1R_s)]}{H_n} \tag{A.5}$$

$$\eta_n = \frac{(1+2n)s_2^n R_s N_n\,[-(1+n)i_n(as_1R_s) + \mu_r X_n(as_1R_s)]}{H_n} \tag{A.6}$$

$$N_n = M_n J_s / j \tag{A.7}$$

$$M_n = \int_{\psi}^{\pi-\psi} \frac{\mu_0}{2}\sqrt{\frac{(2n+1)\pi}{n(n+1)}}\,P_n^1(\cos\theta)\sin\theta\,\mathrm{d}\theta. \tag{A.8}$$

REFERENCES

[1] L. Zhu, J. Guo, and E. Gill, "Review of reaction spheres for spacecraft attitude control," *Prog. Aerosp. Sci.*, vol. 91, pp. 67–86, Apr. 2017. [Online]. Available: http://dx.doi.org/10.1016/j.paerosci.2017.04.001.

[2] W. Haeussermann, "The spherical control motor for three axis attitude control of space vehicles," Tech. Rep. 19630039749, NASA, Washington, D.C., USA, 1959.

[3] A. Chen *et al.*, "Force and torque model utilising transfer-matrix theory for a novel electrodynamic suspension reaction sphere," *IET Electr. Power Appl.*, vol. 12, no. 1, pp. 63–70, 2017.

[4] L. Zhu, J. Guo, and E. Gill, "Scaling effects in miniaturization of reaction spheres," in *Proc. 69th Int. Astronautical Congr.*, Oct. 2018, pp. 1–10.

[5] J. F. P. Fernandes and P. J. C. Branco, "The shell-like spherical induction motor for low-speed traction: Electromagnetic design, analysis, and experimental tests," *IEEE Trans. Ind. Electron.*, vol. 63, no. 7, pp. 4325–4335, Jul. 2016.

[6] M. Cheng, P. Han, G. Buja, and M. G. Jovanovic, "Emerging multiport electrical machines and systems: Past developments, current challenges, and future prospects," *IEEE Trans. Ind. Electron.*, vol. 65, no. 7, pp. 5422–5435, Jul. 2018.

[7] A. Bhatia, M. Kumagai, and R. Hollis, "Six-stator spherical induction motor for balancing mobile robots," in *Proc. IEEE Int. Conf. Robot. Autom.*, 2015, pp. 226–231.

[8] L. Spitzer Jr., "Space telescopes and components," *Astronom. J.*, vol. 65, no. 5, pp. 242–263, Jun. 1960. [Online]. Available: http://dx.doi.org/10.1086/108242.

[9] A. Iwakura, S.-I. Tsuda, and Y. Tsuda, "Feasibility study on three dimensional reaction wheel," *Proc. School Sci. Tokai University, Ser. E*, vol. 33, 2008, pp. 51–57.

[10] Y. Shirasawa and Y. Tsuda, "System performance analysis of three dimensional reaction wheel for the attitude control of microsatellites," *Trans. Japan Soc. Aeronautical Space Sci.*, vol. 7, no. ists26, pp. Pd_105–Pd_110, Dec. 2009. [Online]. Available: http://dx.doi.org/10.2322/tstj.7.Pd_105.

[11] D. Kim, H. Yoon, W. Kang, Y. Kim, and H.-T. Choi, "Development of a spherical reaction wheel actuator using electromagnetic induction," *Aerosp. Sci. Technol.*, vol. 39, pp. 86–94, Dec. 2014. [Online]. Available: http://dx.doi.org/10.1016/j.ast.2014.09.004.

[12] J. Zhang, L.-M. Yuan, S.-L. Chen, C. Zhang, C.-Y. Chen, and J. Zhou, "Design and optimization aspects of a novel reaction sphere actuator," in *Proc. Int. Conf. Intell. Manufacturing Internet Things*, Sep. 2018, pp. 84–93.

[13] Y. Yan, Z. Duan, Q. Zhang, H. Qiao, and C. Gerada, "Development and structure of multi-dof spherical induction motor," in *Proc. 13th IEEE Conf. Ind. Electron. Appl.*, May/Jun. 2018, pp. 2831–2835. [Online]. Available: http://dx.doi.org/10.1109/ICIEA.2018.8398192.

[14] F. Wani, "Three dimensional finite element modeling of a brushless doubly-fed induction machine," M.S. thesis, Delft Univ. Technol., Delft, The Netherlands, 2016.

[15] W. Frei, "How much memory is needed to solve large COMSOL models?" 2014. [Online]. Available: https://www.comsol.com/blogs/much-memory-needed-solve-large-comsol-models, Accessed on: Sep. 26, 2018.

[16] L. Zhu, J. Guo, and E. Gill, "Analytical field and torque analysis of a reaction sphere," *IEEE Trans. Magn.*, vol. 54, no. 12, pp. 1–11, Dec. 2018.

[17] P. C. Sen, *Principles of Electric Machines and Power Electronics*, 3rd ed. Hoboken, NJ, USA: Wiley, 2007.

[18] K. Davey, G. Vachtsevanos, and R. Powers, "The analysis of fields and torques in spherical induction motors," *IEEE Trans. Magn.*, vol. 23, no. 1, pp. 273–282, Jan. 1987.

[19] A. E. Fitzgerald, C. Kingsley, S. D. Umans, and B. James, *Electric Machinery*, 6th ed., vol. 5. New York, NY, USA: McGraw-Hill, 2003.

[20] M. Hoeijmakers, *Modelling of AC Machines ET 4121*. Delft, The Netherlands: Delft Univ. Technol., Apr. 2004.

[21] I. Boldea and S. A. Nasar, *The Induction Machine Handbook*, 1st ed. Boca Raton, FL, USA: CRC Press, Jan. 2002.

[22] S.-J. Lee, J.-M. Kim, D.-K. An, and J.-P. Hong, "Equivalent circuit considering the harmonics of core loss in the squirrel-cage induction motor for electrical power steering application," *IEEE Trans. Magn.*, vol. 50, no. 11, pp. 1–4, Nov. 2014.

[23] X. Liang and Y. Luy, "Harmonic analysis for induction motors," in *Proc. Electr. Comput. Eng. Can. Conf.*, May 2006, pp. 172–177. [Online]. Available: http://dx.doi.org/10.1109/CCECE.2006.277368.

[24] C. Grantham and D. J. McKinnon, "Rapid parameter determination for induction motor analysis and control," *IEEE Trans. Ind. Appl.*, vol. 39, no. 4, pp. 1014–1020, Jul./Aug. 2003.

[25] B. Dehez, V. Froidmont, D. Grenier, and B. Raucent, "Design, modeling and first experimentation of a two-degree-of-freedom spherical actuator," *Robot. Comput.-Integr. Manuf.*, vol. 21, no. 3, pp. 197–204, Jun. 2005.

[26] T. A. Lipo, *Introduction to AC Machine Design*, 1st ed., vol. 63. Hoboken, NJ, USA: Wiley, Oct. 2017.

[27] "Copper data sheet cu-dhp," Deutsches Kupferinstitut, Düsseldorf, Germany.

[28] W. Xu, J. G. Zhu, Y. Zhang, Y. Li, Y. Wang, and Y. Guo, "An improved equivalent circuit model of a single-sided linear induction motor," *IEEE Trans. Veh. Technol.*, vol. 59, no. 5, pp. 2277–2289, Jun. 2010.

Linyu Zhu received the B.Sc. and M.Sc. degrees in aerospace science and technology from Northwestern Polytechnical University, Xi'an, China, in 2012 and 2015, respectively. She is currently working toward the Ph.D. degree in aerospace engineering with the Department of Space Engineering, Delft University of Technology, Delft, The Netherlands.

Her research interests include spacecraft miniaturization, and design and control of reaction spheres.

Jian Guo received the B.Sc. and M.Sc. degrees in engineering from Northwestern Polytechnical University, Xi’an, China, in 1998 and 2001, respectively, and the Ph.D. degree in mechanical engineering from the University of Leeds, Leeds, U.K., in 2010.

He is currently an Assistant Professor with the Department of Space Engineering, Delft University of Technology (TU Delft), Delft, The Netherlands. He is also a Theme Leader of the TU Delft Space Institute. His research interests include small satellites, spacecraft Guidance Navigation and Control, distributed space systems, and space robots.

Eberhard Gill received the Diploma degree in physics from the University of Tübingen, Tübingen, Germany, in 1986, the master’s degree in space systems engineering from the Delft University of Technology (TU Delft), Delft, The Netherlands, in 2005, and the Ph.D. degree in theoretical astrophysics from the University of Tübingen in 1989.

He is currently the Head of the Department of Space Engineering, TU Delft. He is also the Director of the TU Delft Space Institute. His research interests include formation flying, Global Navigation Satellite System, systems engineering, etc.